

Diamond ascent by rift-driven disruption of cratonic mantle keels

Thomas Geron (✉ Thomas.Geron@noc.soton.ac.uk)

University of Southampton <https://orcid.org/0000-0002-7717-2092>

Stephen Jones

University of Birmingham <https://orcid.org/0000-0002-8480-3518>

Sascha Brune

German Research Centre for Geosciences GFZ <https://orcid.org/0000-0003-4985-1810>

Thea Hincks

University of Bristol

Anne Glerum

University of Potsdam

Andrew Merdith

University of Leeds <https://orcid.org/0000-0002-7564-8149>

Martin Palmer

University of Southampton

John Schumacher

Portland State University

Rebecca Primiceri

University of Southampton

Matthew Field

Mining Plus

William Griffin

CCFS/GEMOC <https://orcid.org/0000-0002-0980-2566>

Suzanne O'Reilly

CCFS and GEMOC <https://orcid.org/0000-0002-3883-5498>

Derek Keir

University of Southampton

Christopher Spencer

Queen's University <https://orcid.org/0000-0003-4264-3701>

Physical Sciences - Article

Keywords:

Posted Date: December 8th, 2021

DOI: <https://doi.org/10.21203/rs.3.rs-986686/v1>

License:  This work is licensed under a Creative Commons Attribution 4.0 International License.

[Read Full License](#)

Diamond ascent by rift-driven disruption of cratonic mantle keels

Thomas M. Gernon^{a,*}, Stephen M. Jones^b, Sascha Brune^{c,d}, Thea K. Hincks^a, Anne Glerum^{c,d}, Martin R. Palmer^a, John C. Schumacher^e, Rebecca M. Primiceri^a, Matthew Field^f, William L. Griffin^g, Suzanne Y. O'Reilly^g, Derek Keir^{a,h}, Christopher J. Spencerⁱ, Andrew S. Merdith^j

^a*School of Ocean & Earth Science, University of Southampton, Southampton SO14 3ZH, UK*

^b*School of Geography, Earth & Environmental Sciences, University of Birmingham, Edgbaston, Birmingham B15 2TT, UK*

^c*Helmholtz Centre Potsdam – GFZ German Research Centre for Geosciences, Potsdam, Germany*

^d*University of Potsdam, Potsdam-Golm, Germany*

^e*Department of Geology, Portland State University, Portland, OR, USA*

^f*Mayfield, Wells Road, Wookey Hole Wells, Somerset, BA5 1DN, UK*

^g*GEMOC ARC National Key Centre, Earth and Environmental Sciences Macquarie University NSW 2109, Australia*

^h*Dipartimento di Scienze della Terra, Università degli Studi di Firenze, Florence, Italy*

ⁱ*Department of Geological Sciences and Geological Engineering, Queen's University, Kingston, Canada*

^j*School of Earth and Environment, University of Leeds, Leeds LS2 9TJ, UK*

Diamonds are erupted at Earth's surface in volatile-rich magmas called kimberlites^{1,2,3}. These enigmatic magmas, originating from depths exceeding 150 kilometres in Earth's mantle¹, occur in stable cratons and in pulses broadly synchronous with supercontinent cyclicality⁴. Whether their mobilization is driven by mantle plumes⁵ or mechanical weakening of cratonic lithosphere^{4,6} remains unclear. Here we show that most kimberlites spanning the past billion years erupted approximately 25 million years after the onset of continental fragmentation, suggesting an association with rifting processes. Our dynamic models show that physically steep lithosphere-asthenosphere boundaries formed during terminal rifting (necking) generate convective instabilities in the asthenosphere that slowly migrate many hundreds of kilometres inboard of the rift, causing destabilization of cratonic mantle keel tens of kilometres thick. Displaced lithosphere is replaced by hot, upwelling asthenosphere in the return flow, causing partial melting of carbonated mantle and variable assimilation of lithospheric material. The resulting small-volume kimberlite magmas ascend rapidly and adiabatically, exsolving amounts of carbon dioxide (CO₂) that are consistent with independent constraints⁷. Our model reconciles diagnostic kimberlite features including association with cratons and geochemical characteristics that implicate a common asthenospheric mantle source contaminated by cratonic lithosphere⁸. Together, these results provide a quantitative and mechanistic link between kimberlite episodicity and supercontinent cycles via progressive disruption of cratonic keels.

[1] Over geologic time, pulses of kimberlite magmatism correspond to episodes of global plate reorganization, with comparatively few kimberlite eruptions occurring during periods of supercontinent stability⁴ (Fig. 1a). This synchronicity may suggest that kimberlites are triggered by tectonic disturbances in cratonic lithosphere⁴ or abrupt changes in plate movement⁶. However, this hypothesis does not adequately explain what process stimulates melt generation, and raises a paradox: cratons are defined by their mechanical strength and long-term stability^{9,10,11,12} so should resist tectonic deformation¹³. An alternative model is that kimberlite distributions are controlled by mantle (super-) plumes, possibly linked to large low-shear-velocity provinces (LLSVPs)⁵, which might fertilize, hybridize and even destabilize the cratonic root^{11,14}. This model is, however, hard to reconcile with geochemical characteristics of most kimberlites, which are inconsistent with plume sources¹⁵, and instead require partial melting of convective mantle coupled with assimilation of cratonic lithosphere^{8,15}. Further, strong cratonic keels are thought to divert mantle plumes away from

continental interiors where most kimberlites occur⁹. Testing these models requires both a fully integrated consideration of geodynamics and geochemistry, and an assessment of spatio-temporal dependencies in the global tectonic cycle.

[2] We assessed the link between kimberlites and global tectonics through geologic time using a database of well-dated kimberlites⁶ and a measure of the degree of fragmentation of continental plates from tectonic reconstructions¹⁶. We calculated the rate of change of fragmentation (ΔF) as a proxy for dynamic plate reorganization (Methods; Extended Data Fig. 1), and then calculated multi-million-year time lags¹⁷ between ΔF and the kimberlite count, K , at 1 million year (Myr) intervals (Methods; Fig. 1b). Our cross-correlation analysis reveals a statistically significant association between fragmentation and kimberlites over the past 500 Myrs (Fig. 1b), which persists when we account for auto-correlation in the time series (Extended Data Fig. 2a). The strongest correlation coefficient ($\rho=0.41$) prevails at lags of -26 ± 4 Myr, indicating that continental fragmentation typically leads kimberlite magmatism by 22–30 Myr (Fig. 1b). When we extend our data compilation to 1 Ga (Extended Data Fig. 1), using more uncertain data but

*Corresponding author: Thomas.Gernon@noc.soton.ac.uk

41 capturing two supercontinent cycles (Fig. 1a), the strongest correlation remains at the same lag (Extended Data Fig. 2b). Further, when we account for preservation bias by weighting kimberlite distributions inversely according to surface preservation, the same lag persists (Extended Data Fig. 2c). Thus, the consistent delay between continental breakup and kimberlite magmatism appears to be a genuine feature of the global geodynamic cycle.

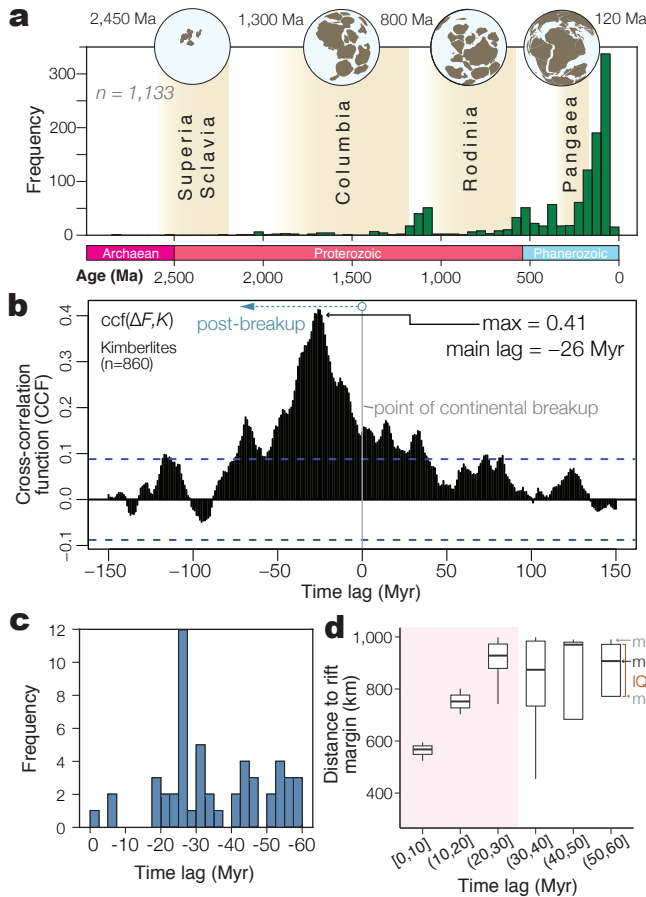


Figure 1. Temporal relationships between tectonics and kimberlites | **a**, Frequency distribution of kimberlites through geologic time (data from ref. 6), showing peaks coinciding with the breakup phase of supercontinent cycles (from ref. 18). **b**, Cross-correlations between ΔF and global kimberlites⁶ spanning 500–0 Ma (Methods), showing dominant time lags at -26 ± 4 Myr (i.e., fragmentation leading kimberlites); positive correlations show that kimberlites are linked to continental fragmentation, not assembly; dashed blue lines show 95% confidence intervals. **c**, Time lags between emplacement of African kimberlite clusters and onset of local rift separation. **d**, Box and whisker plot showing time lags between rift separation and kimberlite eruption versus distance from Atlantic rifted margins ($n=45$; IQR: interquartile range; med: median). Shaded pink field shows a steady increase in distance between rifts and kimberlites in the ~ 30 Myrs following breakup.

49 [3] We scrutinized this linkage further by analyzing spatial¹⁰⁶
50 and temporal lags between kimberlites and continental plate¹⁰⁷
51 margins, targeting the Mesozoic kimberlite fields of southern¹⁰⁸
52 Africa (Fig. 1c). This region is perfectly suited for our purposes¹⁰⁹
53 because the rift kinematics along adjacent plate boundaries are¹¹⁰
54 well constrained at this time¹⁹, and the abundant kimberlites¹¹¹
55 are well understood in terms of their age distributions⁶ and¹¹²

the structure of lithosphere they sample^{20,21,22}. Using plate reconstructions, we measured distances between kimberlites and adjacent rift boundaries (Extended Data Fig. 3) and calculated time lags between rift separation and eruption (Methods). This analysis confirms that a peak in kimberlite emplacement occurs 25–27.5 Myr after the onset of regional breakup (Fig. 1c), corroborating the global result (Fig. 1b). Importantly, we find that kimberlites tend to erupt closer to the rift margins earlier in the rifting cycle—as qualitatively noted before in the São Francisco and Kaapvaal Cratons¹¹—and migrate toward the cratonic interior as fragmentation progresses, initially at a rate of about 18–23 km Myr⁻¹ (Fig. 1d; Methods).

[4] Our results indicate that kimberlite magmatism is strongly associated with continental breakup. However, both breakup^{23,24} and kimberlite magmatism⁵ are commonly attributed to mantle plumes. A crucial question, therefore, is whether rifting itself is the primary driver of kimberlites, or whether mantle plumes drive both rifting and kimberlite magmatism. To address this question, we quantified the relationship between rifting, plumes and kimberlites globally, using the techniques described previously (Methods). We find that the strongest statistically significant correlation between Large Igneous Provinces, LIPs (the accepted main surface expression of mantle plumes)²⁴ and continental fragmentation occurs at $+7 \pm 4$ Myr, i.e., plumes/LIPs lead breakup (Extended Data Fig. 4). Recalling our observation that kimberlites lag breakup by ~ 26 Myr, it at first seems possible that a plume could trigger breakup ~ 7 Myr after impingement, and then kimberlite generation ~ 26 Myr later. However, the lagged correlation between breakup and kimberlites is considerably stronger than that with LIPs, suggesting rifting is the first-order control. Further, the plume model cannot explain our observation that kimberlites tend to erupt closer to the rift boundary earlier in the rifting cycle and migrate inboard of the rift over time. There is no clear mechanism by which plumes could explain this pattern. We therefore conclude that mantle plumes may (or may not) be a primary driver of continental breakup, and may locally warm cratonic keels¹⁴ and deliver ultra-deep diamonds, but it is the breakup process itself that controls most kimberlite magmatism.

[5] This framework then provides two alternatives to explain distal kimberlite eruptions (>500 km from rift margin; Fig. 1d): (i) mechanical stretching of lithosphere; or (ii) increased mantle heat flow linked to rifting. Whilst both processes could perturb the lithosphere-asthenosphere boundary (LAB), destabilizing kimberlite source regions via decompression and heating, we consider a mechanical control unlikely because widespread geologic evidence points to tectonically stable cratonic interiors^{9,10,11,12,13}. Dynamic rifting models underscore the geologic observations, suggesting that the LAB is not mechanically thinned by extension >300 km inboard of rifted margins^{25,26}. We therefore hypothesize that continental breakup drives kimberlite magmatism via a thermal mechanism in the mantle, fundamentally tied to rifting.

[6] Diamond-bearing kimberlites are exclusively found in thick cratons (150–200 km)^{1,3,9,10,13,15}. An inevitable consequence of fragmenting cratons is the generation of a physically steep-sided LAB¹⁴, which should strongly influence man-

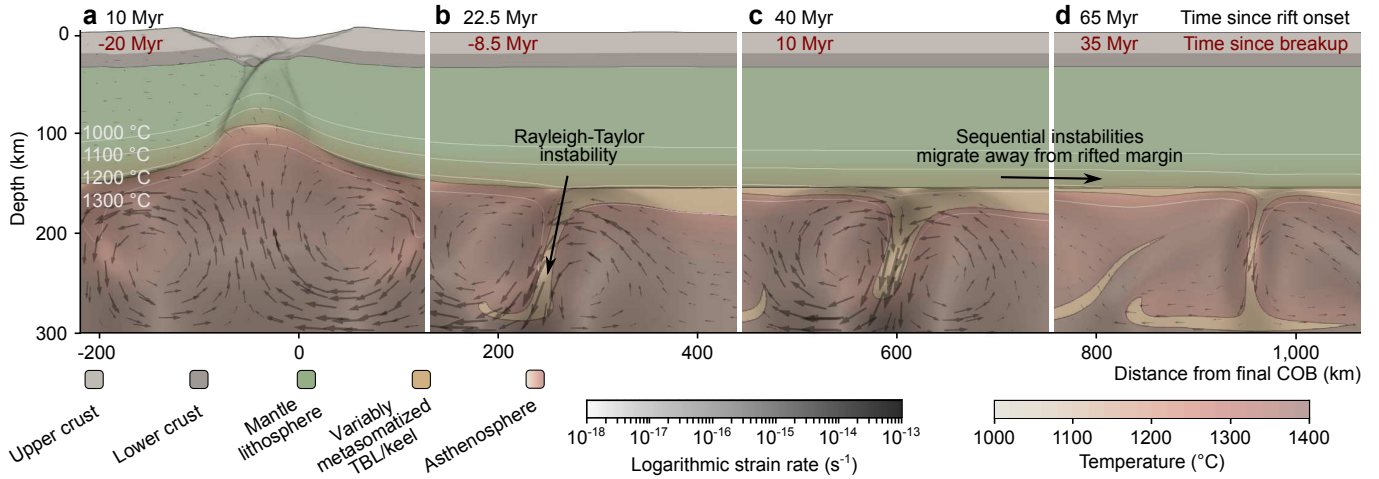


Figure 2. Thermo-mechanical simulations of continental breakup showing generation and propagation of Rayleigh-Taylor instabilities | **a**, Initial rifting causes mantle upwelling (black arrows) and development of steep lithospheric gradients; distance from the continent-ocean boundary (COB) shown along the base, and time since rift onset (black) and breakup (red) along the top (TBL: thermal boundary layer). **b**, Rift necking leads to Rayleigh-Taylor instabilities in the convective mantle, which over time (**c-d**) propagate along the base of cratonic keel, progressively removing the thermal boundary layer. The instability shown migrates at a rate of approximately $15\text{--}20\text{ km Myr}^{-1}$ (Fig. 3a; Extended Data Fig. 6; Supplementary Animation 1). Refer to Methods for details of the model setup.

113 tle flow via edge-driven convection³². Rayleigh-Taylor 148
 114 instability (hereafter, instability) in the lowermost mantle litho-149
 115 sphere, or keel, is a well-described global process^{33,34,35,36,37}.
 116 These instabilities are driven by the density contrast between¹⁵⁰
 117 colder lithosphere and hotter asthenosphere, and metasomatism¹⁵¹
 118 can augment this negative buoyancy driver. Numerical models¹⁵²
 119 demonstrate that convective instabilities are generated by litho-153
 120 spheric edges^{25,26,35}. These instabilities promote upwelling of¹⁵⁴
 121 asthenosphere that feasibly cause melting, convective removal¹⁵⁵
 122 and thinning of lithospheric mantle, which is comparatively¹⁵⁶
 123 cold, dense and heavily veined by metasomatic phases^{14,20,38}
 124 formed potentially over billions of years¹². Petrological obser-158
 125 vations^{14,21,39,40} and dynamic models³⁶ suggest that substan-159
 126 tial erosion/delamination of cratonic keel ($\sim 10\text{s km}$ thick) can¹⁶⁰
 127 occur abruptly (over several Myr)^{11,14}. The question is then¹⁶¹
 128 whether distal rifting can destabilize, and partially melt, cra-162
 129 tonic keel via convective instability.¹⁶³

130 [7] To address this question, we quantified the mechanical¹⁶⁴
 131 and thermal influence of breakup on lithospheric stability us-165
 132 ing two independent and complimentary methods (Figs. 2–3).¹⁶⁶
 133 To investigate the essential physics of the process, we carried¹⁶⁷
 134 out a scaling analysis based on analytical models of viscous¹⁶⁸
 135 instabilities representing the thermal boundary layer between¹⁶⁹
 136 mechanically rigid lithosphere and convecting asthenospheric¹⁷⁰
 137 mantle (Fig. 3a; Methods). To assess the influence of the¹⁷¹
 138 more complex natural geometry and rheology of rifting cratonic¹⁷²
 139 lithosphere, we also carried out more sophisticated numerical¹⁷³
 140 thermo-mechanical simulations (Fig. 2; Methods). Both meth-174
 141 ods predict that necking should trigger initial instabilities in¹⁷⁵
 142 the basal lithosphere beneath the rift shoulder, which crucially¹⁷⁶
 143 then trigger a chain of further instabilities that propagate away¹⁷⁷
 144 from the rift towards the cratonic interior (Fig. 2). The scaling¹⁷⁸
 145 analysis predicts that the horizontal propagation velocity for the¹⁷⁹
 146 chain of instabilities scales as the ratio of the characteristic hor-180
 147 izontal wavelength, λ_d , and the characteristic e-folding growth¹⁸¹

time, τ_d , of individual instabilities. Specifically, the propaga-
 tion velocity (U) is given by

$$U \sim \frac{\lambda_d}{\tau_d} = \lambda_d^* q_d^* \frac{g' b^2}{\nu} \quad (1)$$

where λ_d^* and q_d^* are analytically determined scales for the char-
 acteristic horizontal wavelength and growth rate respectively,
 $g' = g\Delta\rho/\rho$ is reduced gravity, $\Delta\rho$ is the density difference that
 drives the instability relative to asthenospheric density ρ , b is
 the mean starting thickness of the unstable lithospheric root,
 and ν is the kinematic viscosity. Using equation 1, and consid-
 ering lithospheric root thicknesses from xenolith pressure-
 temperature (P - T) estimates (Extended Data Fig. 5), the prop-
 agation velocities are on the order of $14\text{--}26\text{ km Myr}^{-1}$ (Fig.
 3a; Extended Data Table 1a). The simulations confirm how
 migrating convective instability leads to a sequence of progres-
 sive delamination events (Fig. 2; Supplementary Animation 1),
 which migrate beneath the craton at similar rates of $15\text{--}20\text{ km}$
 Myr^{-1} (Extended Data Fig. 6). Both approaches yield propa-
 gation rates that are closely consistent with those estimated
 for kimberlites (Fig. 3a). Further, the characteristic scale of
 instabilities (wavelengths: $50\text{--}90\text{ km}$; Extended Data Table 1a)
 broadly matches those of proposed kimberlite melt sources (10--
 100 km diameter)^{37,41} and kimberlite fields at the surface (30--
 50 km diameter)⁴¹. The thermal Péclet number for return flow
 (Extended Data Table 1a) confirms that asthenosphere will well
 up adiabatically to replace the removed part of keel (Fig. 2), as
 suggested before³⁵.

[8] Hybridization of asthenospheric and lithospheric melts is
 required to explain kimberlite compositions⁸. At pressures con-
 ducive to diamond formation ($\gtrsim 5\text{ GPa}$), the LAB (a thermal
 boundary with an adiabatic temperature of $1,300^\circ\text{C}$) closely
 coincides with the solidus of carbonated mantle^{2,27} (Fig. 3b).
 Hence, whilst cratons are anomalously cold and stable over
 billions of years^{9,11}, minor changes in pressure and temper-

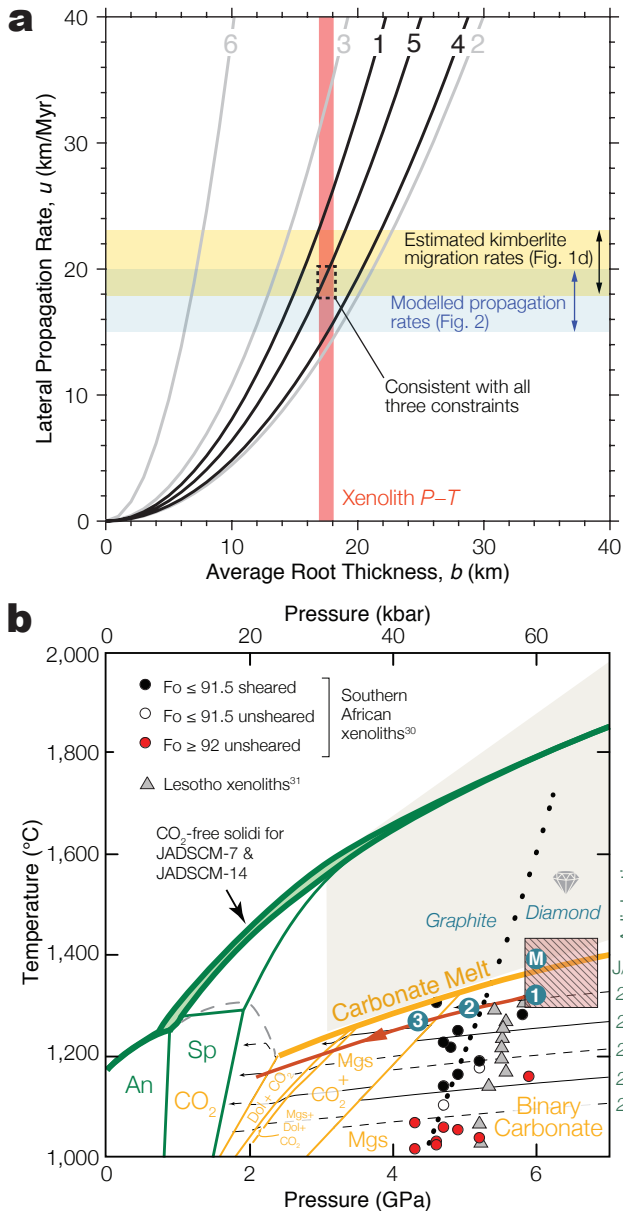


Figure 3. Models of instability migration and conditions of melt generation | **a**, Lateral propagation rates for Rayleigh-Taylor instabilities as defined by equation 1 for six analytical fluid dynamical models (Extended Data Table 1a). Models 1, 4 and 5 (black lines) are most applicable, and describe a dense, viscous layer representing the lithospheric keel that overlies a less dense, viscous half-space representing asthenosphere. A kinematic viscosity of $7 \times 10^{15} \text{ m}^2 \text{ s}^{-1}$ gives good agreement with constraints from kimberlite migration (Fig. 1d), numerical simulations of basal lithospheric instabilities (Fig. 2), and lithospheric root thicknesses inferred from modelling xenolith P - T data. **b**, Phase diagram showing carbonate-bearing lherzolite solidi (solid orange line) for proposed kimberlite starting compositions, JADSCM-7 and JADSCM-14²⁷; shaded area shows the $\text{CaO-MgO-Al}_2\text{O}_3\text{-SiO}_2\text{-CO}_2$ (CMAS- CO_2) field of carbonatite and kimberlite melt generation from refs.^{27,28}; hatched box shows P - T conditions in the thermal boundary layer, derived from analysis of xenolith geotherms (Extended Data Fig. 5); Dol=dolomite, Mgs=magnesite, Sp=spinel, Grt=garnet, An=anorthite. The graphite-diamond phase boundary is from ref.²⁹. Xenolith P - T estimates for various southern African³⁰ and Lesotho³¹ kimberlites are plotted, distinguishing olivine forsterite (Fo) contents as a measure of fertility (black are more fertile and typically sheared, signifying high- T conditions; Extended Data Fig. 7). Adiabatic P - T paths for fixed composition are shown, as is the probable melt pathway (red arrow; points 1–3); corresponding phase modes are shown in Extended Data Fig. 8d.

182 ature can generate the characteristically small-volume⁴¹ CO_2
 183 and H_2O -rich melts parental to kimberlites^{2,27,28,42,43}. Our
 184 instability modelling confirms that convective delamination of
 185 the keel allows asthenosphere to migrate adiabatically to shall-
 186 lower depths of 150–170 km and lower pressures of 5–5.5 GPa
 187 (Figs. 2–3; Extended Data Table 1a). Importantly, the simula-
 188 tions show that domains of the detached lithospheric keel are
 189 entrained in the upwelling asthenospheric return flow (Fig. 2;
 190 Supplementary Animation 1). Convective delamination will
 191 be aided by modal metasomatism (refertilization, where new
 192 minerals are formed)—a continent-scale pervasive effect⁴⁴ that
 193 can destabilize the keel^{21,39,45}. For example, dense, high-Fe
 194 (low forsterite, Fo) peridotites are thought to have formed dur-
 195 ing high-temperature melt-metasomatism shortly prior to erup-
 196 tion³⁹. These xenoliths (typically sheared)^{30,31} occur in a 20–
 197 25 km-thick zone near the LAB at ~ 5 GPa (Fig. 3b; Extended
 198 Data Fig. 7). Such compositional changes are expected to in-
 199 crease the bulk density by several percent^{39,45} relative to low-
 200 density melt-depleted keel¹³, making it particularly prone to
 201 delamination^{21,39,45}. Thus, we hypothesize that upwelling CO_2 -
 202 bearing garnet lherzolite (Fig. 2) warms, refertilizes and weak-
 203 ens the cratonic keel¹⁴, which may prompt further delamina-
 204 tion.

205 [9] Our modelling suggests that the entrained, metasoma-
 206 tized lithospheric keel (Fig. 2) could be an important contrib-
 207 utor of carbonate and hydrous phases to the kimberlite man-
 208 tle source^{2,3,7,37}. Assuming these phases are present in the
 209 source, we calculate that up to 1% decompressional melting
 210 occurs within the upwelling limbs of instabilities beneath thick
 211 lithosphere (Methods; Extended Data Fig. 8). Upwelling within
 212 each convective instability can potentially generate 10s to 100s
 213 km^3 of magma over its lifetime (Extended Data Fig. 8b), which
 214 is sufficient to explain estimated volumes of kimberlite erup-
 215 tions³⁷. The resulting small-volume kimberlite melts ascend
 216 rapidly and adiabatically (Fig. 3b). Decarbonation^{27,28,42} oc-
 217 curs between 5 and 3 GPa (Fig. 3b), driving off 4–7 wt%
 218 CO_2 (Extended Data Fig. 8d) and accelerating kimberlite as-
 219 cent (thus aiding diamond preservation). Numerical models in-
 220 dicate that kimberlites with exsolved CO_2 contents of ≥ 5 wt%
 221 are eruptible⁷.

222 [10] Our models suggest that convective instabilities can
 223 erode/delaminate several tens of kilometres of cratonic keel,
 224 which should be detectable using geochemical and geophysical
 225 constraints. Taking southern Africa as an example, geochemi-
 226 cal studies of peridotitic xenoliths and garnet xenocrysts inde-
 227 pendently invoke loss of 30–40 km lithosphere during the mid-
 228 Cretaceous^{40,46}, coinciding with the surge in kimberlite volca-
 229 nism (Fig. 1a). This removal is supported by the realignment of
 230 lower lithospheric anisotropy since the Mesozoic¹¹. The re-
 231 moved thickness closely matches both our empirically derived
 232 thickness of lithospheric thermal boundary layer (~ 35 km; Ex-
 233 tended Data Fig. 5), and the intensely melt-metasomatized root
 234 of the Kaapvaal Craton^{20,21,22}. This suggests that these layers at
 235 least partly overlap, as has been proposed²⁰, and that further de-
 236 coupling of keel may occur due to chemical/mechanical weak-
 237 nesses^{11,14} and increased density tied to refertilization^{21,39,45}.

238 [11] This hypothesis is also testable by studying time-

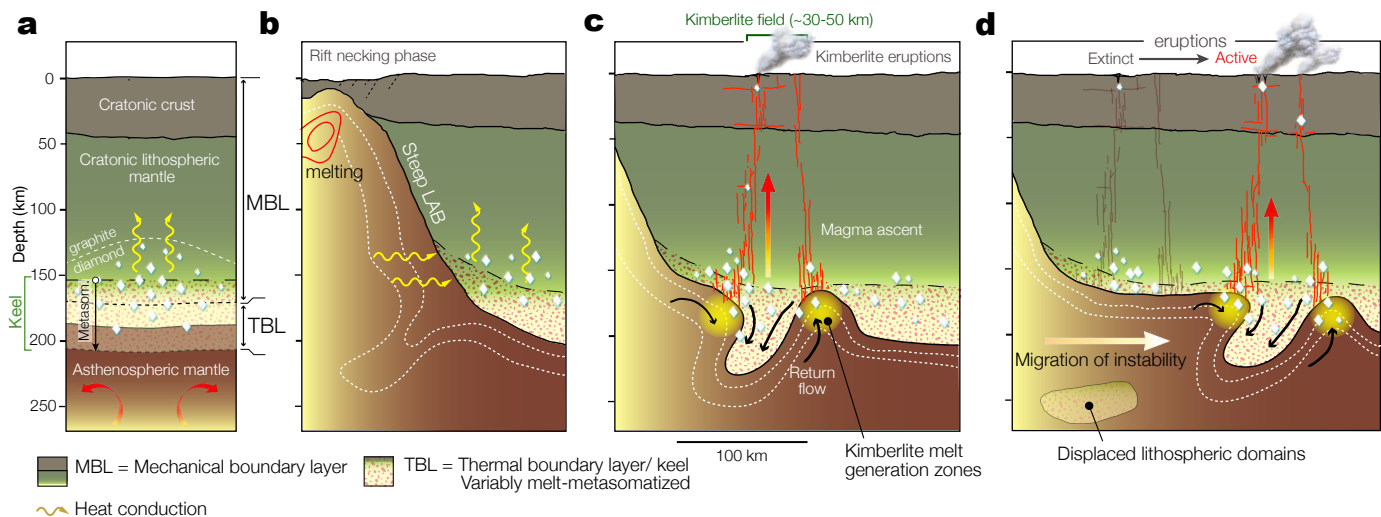


Figure 4. Far-field effects of rifting on cratonic mantle keel stability through time | **a**, Simplified craton structure showing mechanical and thermal boundary layers. **b**, Rifting generates a steep lithospheric gradient that gives rise to Rayleigh-Taylor instability (Fig. 2), coeval with necking (dashed white lines depict schematic isotherms). **c**, Migration, continued growth and detachment of the instability. The return flow (black arrow) warms and refertilizes the keel, causing sharp increases in density and, ultimately, decoupling. Low-density asthenosphere wells up adiabatically to replace removed keel causing partial melting of (and mixing with) metasomatized lithospheric mantle. Resulting small-volume kimberlitic magmas ascend adiabatically to erupt at Earth's surface. **d**, The process repeats: destabilization, and removal, of cratonic keel propagates inboard of the rift leading to migration of kimberlite volcanism. The intensity of lithospheric assimilation declines over time: late-stage melting is dominated by asthenospheric mantle once the cratonic keel has foundered or been exhausted during early melting (Supplementary Animation 1).

integrated variations in kimberlite geochemistry, which should reflect changes in the degree of lithospheric assimilation tied to convective removal. Notably, there is evidence for a fundamental shift in kimberlite compositions that coincides with abrupt lithospheric disruption in Mesozoic southern Africa: a step change in compositions from those initially exhibiting strong lithospheric/metamorphic enrichment ('Group 2' kimberlites or lamproites)⁴⁷ to those exhibiting stronger asthenospheric signatures ('Group 1' kimberlites)⁴⁷ (Extended Data Fig. 9). The petrogenesis of later 'Group 1' kimberlites implies shallower, hotter melting conditions at 150–160 km depth, in many cases only several Myr after melting dominated by lithospheric assimilation at ~200 km depth⁴⁰. These abrupt geochemical changes are best explained by delamination. We infer that the restriction of Group 2 kimberlites to the main phase of Gondwana breakup (200–110 Ma)⁴⁸ is related to progressive exhaustion of metasomatized material due to foundering of keel associated with instabilities (Fig. 4). This process is naturally then followed by eruption of melts with stronger asthenospheric signatures⁴³, as detected independently by changes in isotope chemistry^{47,49} and coeval abrupt shifts in the Ti contents of garnet xenocrysts⁴⁰ (Extended Data Fig. 9).

[12] Our analysis supports the emerging consensus that most kimberlites originate as a mixture of volatile-rich melts from both asthenospheric and lower lithospheric mantle^{8,15,50}. Previous models do not satisfactorily explain what process suddenly generates and extracts these melts. Our data and observations indicate that plumes from LLSVPs might initiate continental breakup, with rifting then driving mantle instabilities that erode cratonic keel, prompting much later (~10s Myr) feedbacks between heat transfer, melt generation and extraction (Fig. 4). The rates of laterally migrating Rayleigh-Taylor instabilities closely

match those of kimberlite magmatism into the cratonic interior as continental breakup progresses (Fig. 3a). This fits with previous thermochronological evidence for systematic removal of Kaapvaal lithospheric root progressively from craton margins towards the interior¹¹. Our statistical analysis of observations coupled with numerical and thermodynamic modelling explains the dichotomy between kimberlites and LLSVPs being spatially correlated⁵, despite most kimberlite compositions (and their xenoliths⁴⁶) globally being inconsistent with derivation from plume sources^{8,15}. Taken together, our results suggest that diamond-bearing kimberlite magmas are mobilized by the far-field thermal effects of rift tectonics during the breakup phase of supercontinent cycles.

Online content

Any methods, additional references, Nature Research reporting summaries, source data, extended data, supplementary information, acknowledgements, peer review information; details of author contributions and competing interests; and statements of data and code availability are available at <https://doi.org/10.1038/s12345-111-2222-3>.

References

1. R.H. Mitchell. *Kimberlites: Mineralogy, Geochemistry, and Petrology*. Springer Science and Business Media, New York, 1986.
2. R. S. J. Sparks, L. Baker, R. J. Brown, M. Field, J. Schumacher, G. Stripp, and A. Walters. Dynamical constraints on kimberlite volcanism. *Journal of Volcanology and Geothermal Research*, 155(1):18–48, 2006.
3. J. K. Russell, L. A. Porritt, Y. Lavallée, and D. B. Dingwell. Kimberlite ascent by assimilation-fuelled buoyancy. *Nature*, 481(7381):352–356, 2012.

4. H. Jelsma, W. Barnett, S. Richards, and G. Lister. Tectonic setting of kimberlites. *Lithos*, 112:155–165, 2009.
5. T. H. Torsvik, K. Burke, B. Steinberger, S. J. Webb, and L. D. Ashwal. Diamonds sampled by plumes from the core–mantle boundary. *Nature*, 466(7304):352–355, 2010.
6. S. Tappe, K. Smart, T. Torsvik, M. Massuyeau, and M. de Wit. Geodynamics of kimberlites on a cooling Earth: Clues to plate tectonic evolution and deep volatile cycles. *Earth and Planetary Science Letters*, 484:1–14, 2018.
7. J. L. Kavanagh and R. S. J. Sparks. Temperature changes in ascending kimberlite magma. *Earth and Planetary Science Letters*, 286(3):404–413, 2009.
8. A. Giuliani, D. G. Pearson, A. Soltys, H. Dalton, D. Phillips, S. F. Foley, E. Lim, K. Goemann, W. L. Griffin, and R. H. Mitchell. Kimberlite genesis from a common carbonate-rich primary melt modified by lithospheric mantle assimilation. *Science Advances*, 6(17):eaaz0424, 2020.
9. D. G. Pearson, J. M. Scott, J. Liu, A. Schaeffer, L. H. Wang, J. van Hunen, K. Szilas, T. Chacko, and P. B. Kelemen. Deep continental roots and cratons. *Nature*, 596(7871):199–210, 2021.
10. N. L. Celli, S. Lebedev, A. J. Schaeffer, and C. Gaina. African cratonic lithosphere carved by mantle plumes. *Nature Communications*, 11(1):92, 2020.
11. J. Hu, L. Liu, M. Faccenda, Q. Zhou, K. M. Fischer, S. Marshak, and C. Lundstrom. Modification of the Western Gondwana craton by plume–lithosphere interaction. *Nature Geoscience*, 11(3):203–210, 2018.
12. F. A. Capitanio, O. Nebel, and P. A. Cawood. Thermochemical lithosphere differentiation and the origin of cratonic mantle. *Nature*, 588(7836):89–94, 2020.
13. A. L. Perchuk, T. V. Gerya, V. S. Zakharov, and W. L. Griffin. Building cratonic keels in Precambrian plate tectonics. *Nature*, 586(7829):395–401, 2020.
14. S. F. Foley. Rejuvenation and erosion of the cratonic lithosphere. *Nature Geoscience*, 1(8):503–510, 2008.
15. S. Tappe, N. B. Brand, A. Stracke, D. van Acken, C.-Z. Liu, H. Strauss, F.-Y. Wu, A. Luguët, and R. H. Mitchell. Plates or plumes in the origin of kimberlites: U/Pb perovskite and Sr-Nd-Hf-Os-C-O isotope constraints from the Superior craton (Canada). *Chemical Geology*, 455:57–83, 2017.
16. A. S. Merdith, S. E. Williams, S. Brune, A. S. Collins, and R. D. Müller. Rift and plate boundary evolution across two supercontinent cycles. *Global and Planetary Change*, 173:1–14, 2019.
17. T. M. Gernon, T. K. Hincks, A. S. Merdith, E. J. Rohling, M. R. Palmer, G. L. Foster, C. P. Bataille, and R. D. Müller. Global chemical weathering dominated by continental arcs since the mid-Palaeozoic. *Nature Geoscience*, 14(9):690–696, 2021.
18. R. N. Mitchell, N. Zhang, J. Salminen, Y. Liu, C. J. Spencer, B. Steinberger, J. B. Murphy, and Z.-X. Li. The supercontinent cycle. *Nature Reviews Earth & Environment*, 2(5):358–374, 2021.
19. S. Brune, S. E. Williams, N. P. Butterworth, and R. D. Müller. Abrupt plate accelerations shape rifted continental margins. *Nature*, 536(7615):201–204, 2016.
20. W. L. Griffin, S. Y. O’Reilly, J. C. Afonso, and G. C. Begg. The composition and evolution of lithospheric mantle: a re-evaluation and its tectonic implications. *Journal of Petrology*, 50(7):1185–1204, 2009.
21. G. C. Begg, W. L. Griffin, L. M. Natapov, Suzanne Y. O’Reilly, S. P. Grand, C. J. O’Neill, J. M. A. Hronsky, Y. Poudjom Djomani, C. J. Swain, T. Deen, and P. Bowden. The lithospheric architecture of Africa: Seismic tomography, mantle petrology, and tectonic evolution. *Geosphere*, 5(1):23–50, 2009.
22. S. Y. O’Reilly and W. L. Griffin. Mantle metasomatism. In D. E. Harlow and H. Austrheim, editors, *Metasomatism and the Chemical Transformation of Rock: The Role of Fluids in Terrestrial and Extraterrestrial Processes*, pages 471–533. Springer Berlin Heidelberg, Berlin, Heidelberg, 2013.
23. B. C. Storey. The role of mantle plumes in continental breakup: case histories from Gondwanaland. *Nature*, 377(6547):301–308, 1995.
24. R. E. Ernst. *Large igneous provinces*. Cambridge University Press, 2014.
25. R. Huismans and C. Beaumont. Depth-dependent extension, two-stage breakup and cratonic underplating at rifted margins. *Nature*, 473(7345):74–78, 2011.
26. W. Gorczyk and C. M. Gonzalez. CO₂ degassing and melting of metasomatized mantle lithosphere during rifting—Numerical study. *Geoscience Frontiers*, 10(4):1409–1420, 2019.
27. G. H. Gudfinnsson and D. C. Presnall. Continuous gradations among primary carbonatitic, kimberlitic, melilititic, basaltic, picritic, and komatiitic melts in equilibrium with garnet lherzolite at 3–8 GPa. *Journal of Petrology*, 46(8):1645–1659, 2005.
28. J. A. Dalton and D. C. Presnall. The continuum of primary carbonatitic–kimberlitic melt compositions in equilibrium with lherzolite: Data from the system CaO–MgO–Al₂O₃–SiO₂–CO₂ at 6 GPa. *Journal of Petrology*, 39(11-12):1953–1964, 1998.
29. H. W. Day. A revised diamond–graphite transition curve. *American Mineralogist*, 97:52–62, 2012.
30. V. Baptiste, A. Tommasi, and S. Demouchy. Deformation and hydration of the lithospheric mantle beneath the Kaapvaal craton, South Africa. *Lithos*, 149:31–50, 2012.
31. F. R. Boyd and P. H. Nixon. Origin of the ilmenite-silicate nodules in kimberlites from Lesotho and South Africa. In P. H. Nixon, editor, *Lesotho Kimberlites*, pages 254–268. Lesotho National Development Corp, Maseru, Lesotho, 1973.
32. S. D. King and D. L. Anderson. Edge-driven convection. *Earth and Planetary Science Letters*, 160(3):289–296, 1998.
33. W. R. Buck. Small-scale convection induced by passive rifting: the cause for uplift of rift shoulders. *Earth and Planetary Science Letters*, 77(3):362–372, 1986.
34. C. P. Conrad and P. Molnar. The growth of Rayleigh–Taylor-type instabilities in the lithosphere for various rheological and density structures. *Geophysical Journal International*, 129(1):95–112, 1997.
35. J. W. van Wijk, W. S. Baldrige, J. van Hunen, S. Goes, R. Aster, D. D. Coblenz, S. P. Grand, and J. Ni. Small-scale convection at the edge of the Colorado Plateau: Implications for topography, magmatism, and evolution of Proterozoic lithosphere. *Geology*, 38(7):611–614, 2010.
36. W. Gorczyk, B. Hobbs, and T. Gerya. Initiation of Rayleigh–Taylor instabilities in intra-cratonic settings. *Tectonophysics*, 514-517:146–155, 2012.
37. J. K. Russell, R. S. J. Sparks, and J. L. Kavanagh. Kimberlite volcanology: Transport, ascent, and eruption. *Elements*, 15(6):405–410, 2019.
38. S. Y. O’Reilly and W. L. Griffin. Imaging global chemical and thermal heterogeneity in the subcontinental lithospheric mantle with garnets and xenoliths: Geophysical implications. *Tectonophysics*, 416(1):289–309, 2006.
39. Y. H. Poudjom Djomani, S. Y. O’Reilly, W. L. Griffin, and P. Morgan. The density structure of subcontinental lithosphere through time. *Earth and Planetary Science Letters*, 184(3):605–621, 2001.
40. A. F. Kobussen, W. L. Griffin, S. Y. O’Reilly, and S. R. Shee. Ghosts of lithospheres past: Imaging an evolving lithospheric mantle in southern Africa. *Geology*, 36(7):515–518, 2008.
41. M. Grégoire, M. Rabinowicz, and A. J. A. Janse. Mantle mush compaction: A key to understand the mechanisms of concentration of kimberlite melts and initiation of swarms of kimberlite dykes. *Journal of Petrology*, 47(3):631–646, 2006.
42. P. J. Wyllie and W. L. Huang. Carbonation and melting reactions in the system CaO–MgO–SiO₂–CO₂ at mantle pressures with geophysical and petrological applications. *Contributions to Mineralogy and Petrology*, 54(2):79–107, 1976.
43. N. T. Arndt, M. Guitreau, A. M. Boullier, A. Le Roex, A. Tommasi, P. Cordier, and A. Sobolev. Olivine, and the origin of kimberlite. *Journal of Petrology*, 51(3):573–602, 2010.
44. J. Woodhead, J. Hergt, A. Giuliani, D. Phillips, and R. Maas. Tracking continental-scale modification of the Earth’s mantle using zircon megacrysts. *Geochemical Perspectives Letters*, 4:1–6, 2017.
45. W. L. Griffin and S. Y. O’Reilly. Cratonic lithospheric mantle: Is anything subducted? *Episodes*, 30(1):43–53, 2007.
46. P. E. Janney, S. B. Shirey, R. W. Carlson, D. G. Pearson, D. R. Bell, A. P. Le Roex, A. Ishikawa, P. H. Nixon, and F. R. Boyd. Age, composition and thermal characteristics of South African off-craton mantle lithosphere: Evidence for a multi-stage history. *Journal of Petrology*, 51(9):1849–1890, 2010.
47. C. B. Smith. Pb, Sr and Nd isotopic evidence for sources of southern African Cretaceous kimberlites. *Nature*, 304(5921):51–54, 1983.
48. E.M.W. Skinner. Contrasting Group 1 and Group 2 kimberlite petrology: Towards a genetic model for kimberlites. In *4th International Kimberlite Conference: Extended Abstracts*, volume 4, pages 202–204, 1986.

49. J. Woodhead, J. Hergt, D. Phillips, and C. Paton. African kimberlites revisited: In situ Sr-isotope analysis of groundmass perovskite. *Lithos*, 112:311–317, 2009.
50. S. Tappe, D. G. Pearson, G. Nowell, T. Nielsen, P. Milstead, and K. Muehlenbachs. A fresh isotopic look at Greenland kimberlites: Cratonic mantle lithosphere imprint on deep source signal. *Earth and Planetary Science Letters*, 305(1):235–248, 2011.

Acknowledgements

T.G. and T.H. were supported by The Alan Turing Institute under the EPSRC grant EP/N510129/1. T.G. and R.M.P. received support from the Web Science Institute Stimulus Fund with IBM United Kingdom. A.S.M. was supported by the MCSA Fellowship NEOEARTH, project 893615. We thank Ritske Huisman for helpful discussions, and Steve Sparks and Ross Mitchell for comments on an earlier version of the manuscript. We also acknowledge the late Maarten de Wit for many stimulating discussions on Gondwana breakup and Kaapvaal kimberlites.

Author contributions

T.G. conceived the idea, interpreted data and prepared the manuscript. S.M.J. developed the analytical model of Rayleigh-Taylor instability and performed geotherm and melting calculations. S.B. developed the thermo-mechanical simulations, with input from A.G. who contributed expertise in *ASPECT* modelling. T.H. carried out statistical analysis and modelling with T.G. D.K. and R.M.P. contributed geotectonic interpretations, and A.M. provided support with plate tectonic modelling software, *GPlates* and *pyGPlates* (<https://www.gplates.org/>). M.F. contributed expertise on kimberlites. S.Y.O. and W.L.G. helped analyze and interpret xenolith data and lithospheric processes. J.C.S. contributed expertise in phase diagrams, phase equilibria, and thermodynamic data, using the open-source *Perple_X* software (<https://www.perplex.ethz.ch/>). M.P. and C.J.S. analyzed and interpreted geochemical data. T.G. and S.M.J. wrote the manuscript with input from all co-authors.

284 Methods

285 *Statistical analysis of geotectonics and kimberlites*

286 To quantitatively understand the link between kimber-³⁴¹
 287 lites and continental breakup, we used a global database of³⁴²
 288 radiometrically-dated kimberlites⁶ and a quantitative measure³⁴³
 289 of the degree of fragmentation of the continental plate system³⁴⁴
 290 over geologic time¹⁶ derived from plate tectonic reconstruc-³⁴⁵
 291 tions⁵¹. This method involves the calculation of a continental³⁴⁶
 292 perimeter-to-area ratio, whereby during supercontinent stabil-³⁴⁷
 293 ity, the ratio should be low, whereas during assembly and dis-³⁴⁸
 294 persal it should be high¹⁶ (Extended Data Fig. 1). This variable³⁴⁹
 295 is not necessarily sensitive to active breakup processes (that³⁵⁰
 296 is, the value remains high even after supercontinent breakup³⁵¹
 297 is complete). To account for this, we next calculated the rate³⁵²
 298 of change of fragmentation (ΔF). We did this by calculating the³⁵³
 299 slope of the regression line using a symmetric, moving window³⁵⁴
 300 of ± 4 Myr through the fragmentation time series (Extended³⁵⁵
 301 Data Fig. 1c–d). We next calculated the statistical relation-³⁵⁶
 302 ship between the kimberlite distribution (Extended Data Fig.³⁵⁷
 303 1a–b) and ΔF . Figure 1b shows the cross-correlation function³⁵⁸
 304 (CCF) between these two data series computed in *R* (using the³⁵⁹
 305 function *acf* in Stats package) for lags up to ± 150 Myr. *ccf*(*x*,³⁶⁰
 306 *y*) computes the empirical (Pearson) correlations between two³⁶¹
 307 time-series *x* and *y* at different lags (offsets), where the lag *k*³⁶²
 308 value is the correlation between $x[t+k]$ and $y[t]$. The dashed³⁶³
 309 line (Fig. 1b) shows the approximate 95% confidence interval³⁶⁴
 310 $t=0.088$ ($n=500$ observations), calculated using³⁶⁵

$$311 \quad t = qnorm\left(\frac{1+C}{2}\right) \frac{1}{\sqrt{n}} \quad (2) \quad 312$$

313 where *qnorm* is the quantile function for the normal distribu-³⁷⁰
 314 tion, $C=0.95$ and $n=500$.³⁷¹

315 To further test the estimated ~ 26 Myr lag between changes³⁷²
 316 in fragmentation and kimberlite eruption (Fig. 1b) we incor-³⁷³
 317 porated these measures into a Bayesian network, using an ap-³⁷⁴
 318 proach developed using *UNINET*—a software package for high³⁷⁵
 319 dimensional-dependence modelling—previously used for anal-³⁷⁶
 320 ysis of tectonic and geochemical processes across different spa-³⁷⁷
 321 tial and temporal scales¹⁷. We constructed a simple Bayesian³⁷⁸
 322 network to calculate conditional rank correlations at increasing³⁷⁹
 323 lags from 0 to 50 Myr. Unlike the standard CCF, this accounts³⁸⁰
 324 for the prior effects of shorter lags, similar to the Partial Auto³⁸¹
 325 or Cross Correlation. Inputs are a 1 Myr time-series for the³⁸²
 326 kimberlite count (K_t) from 500 Ma to present (i.e., number of³⁸³
 327 recorded kimberlite events per Myr), and ΔF at lead times 0–50³⁸⁴
 328 Myr before kimberlite eruption (in increments of 5 Myr). The³⁸⁵
 329 average rate of change at a given point in time is the slope of the³⁸⁶
 330 regression line from a symmetric, moving window of ± 4 Myr.³⁸⁷

331 As we are interested in the correlation of (lagged) ΔF with³⁸⁸
 332 K_t , and wish to remove the effects of shorter lags at each step³⁸⁹
 333 (e.g., see ref.¹⁷), we define the Bayesian network node hierar-³⁹⁰
 334 chy as: $\Delta F_t, \Delta F_{t-5}, \Delta F_{t-10}, \dots, \Delta F_{t-50}, K_t$; where ΔF_{t-5} is the³⁹¹
 335 time-series for ΔF offset by $t-5$ (i.e., ΔF leading K_t). These³⁹²
 336 nodes are used to construct a saturated BN: a network in which³⁹³
 337 each node is connected by an arc to every other node in the³⁹⁴

338 network. Using *UNINET*, we can then compute the rank corre-
 339 lation of ΔF_t and K_t (lag 0), the rank correlation of ΔF_{t-5} and K_t
 340 conditional on ΔF_t , the rank correlation of ΔF_{t-10} and K_t con-
 341 ditional on ΔF_t and ΔF_{t-5} , etc. (Extended Data Fig. 2a). This
 342 gives a peak conditional correlation (0.51) at ~ 25 Myr (with an
 343 uncertainty of approximately ± 4 Myr due to the moving win-
 344 dow used to calculate ΔF), in keeping with the results of mod-
 345 elling and observations (Fig. 1). We repeated the above proce-
 346 dure to analyze the relationship between ΔF and large igneous
 347 provinces (LIPs) using the well-established ages of LIP mag-
 348 matism from ref.²⁴ (Extended Data Fig. 4). Here, the input is a
 349 5 Myr resolution series, where *LIPstart* is the total number of
 350 LIP events with a start date falling in each 5 Myr interval, and
 351 ΔF is the slope of the regression line for continental fragmenta-
 352 tion (over a 9 Myr window) again estimated every 5 Myr. Using
 353 a simple saturated BN, we compute the correlation of ΔF and
 354 *LIPstart*, or $\text{corr}(\Delta F, \text{LIP})$ — i.e., where *LIPstart* precedes ΔF
 355 (Extended Data Fig. 4b).

356 We next evaluated the relationship between continental
 357 breakup and kimberlite magmatism, taking Mesozoic Africa
 358 as a regional case study, where data confidence (e.g., kimber-
 359 lites and rifting history) is high. Here, we utilized paleogeog-
 360 raphic reconstructions in the open-source plate tectonic mod-
 361 elling software, *GPlates*⁵¹. We measured the distance and time
 362 lags between kimberlites (using their radiometric ages⁶) and
 363 the margins of neighbouring, coeval rift systems—using the
 364 mapped extent of continent-ocean boundaries through time⁵¹
 365 (Extended Data Fig. 3). Distances were calculated using the
 366 *dist2Line* function from the *R* package, *geosphere*. This cal-
 367 culates the shortest distance (in meters) between points and
 368 polylines or polygons with longitude/latitude coordinates. The
 369 COB shapefile comprises polylines with an attribute *RiftAge* de-
 370 noting the age of separation of each individual section of rift.
 371 We focussed our attention on the three major rift systems ad-
 372 jacent to the kimberlite clusters: the South Atlantic, Africa-
 373 Madagascar/Africa-Antarctica, and Central Atlantic (Extended
 374 Data Fig. 3). For each known *RiftAge*, *t*, we identify all the
 375 kimberlites that are the same age or younger. We then find the
 376 shortest distance from each kimberlite (point coordinates) to a
 377 rift with *RiftAge* = *t*. This gives a set of potential time lags from
 378 initiation of rifting to kimberlite eruption. As a kimberlite could
 379 potentially be associated with a number of rift sections, and we
 380 want to find most likely (the unambiguously closest in time and
 381 distance) we set a maximum lag of 60 Myr and a maximum
 382 distance of $1e6$ m (1,000 km), capturing the ‘craton-scale’³⁷
 383 (Extended Data Fig. 3). We then eliminate any remaining du-
 384 plicate cases so a single kimberlite is only counted once, and
 385 associated with an individual rift section.

386 To estimate the rate of kimberlite migration into the cratonic
 387 interior, we used the steady increase in distance between rifted
 388 margins and kimberlites in the ~ 30 Myr following continental
 389 fragmentation (Fig. 1d). Kimberlites can only form where the
 390 craton is sufficiently thick (≥ 150 km) so migration starts some
 391 distance (i.e., several hundred kilometres) inboard of the rift
 392 margin. Assuming an LAB angle of 40° beneath the rift (in-
 393 spired by models of ref.²⁵), the sharp lithospheric edge must
 394 occur at least ~ 250 km inboard of the rift, which is broadly

in agreement with our models (Fig. 2). In regions such as the Kaapvaal Craton, however, the surface boundary of the craton is located at least 400 km inboard of the rift. Therefore, taking the range 250 to 400 km as realistic starting distances for kimberlites yields migration rates of 23 km Myr⁻¹ and 18 km Myr⁻¹, respectively. Notably, these rates are similar to our modelled propagation rates of Rayleigh-Taylor instabilities (Fig. 3a).

Scaling analysis of Rayleigh-Taylor instability chains

Motivated by the observation that kimberlite magmatism migrates laterally over time, we investigated whether an initial convective instability in the basal lithosphere can trigger further instabilities in an organised manner. We developed a simple physical model for spatial and temporal organization within a series of Rayleigh-Taylor instabilities based on analytical models for individual instabilities, and derived a scaling law for the lateral propagation rate of an instability chain.

The thermal boundary between the lithosphere and asthenosphere can be represented by a simple model of a viscous fluid layer of thickness b representing lithospheric keel that overlies a less dense viscous fluid representing asthenospheric mantle. Analytical solutions for Rayleigh-Taylor instability are available for a starting situation where the interface between the two fluids has a sinusoidal displacement of horizontal wavelength λ and amplitude w_0 , and $w_0 \ll \lambda$. The amplitude of an instability grows as

$$w = w_0 e^{qt} \quad (3)$$

where q is the growth rate. The solutions give the scaled horizontal wavelength of the fastest growing instability, λ_d^* , and the corresponding scaled growth rate, q_d^* . For the geologically relevant solutions of interest, λ_d^* is 2–4 and q_d^* is of order 10⁻¹ (Extended Data Table 1a).

To apply these analytical solutions, note that length is scaled by the mean starting layer thickness, b , and time is scaled by $\nu/g'b$, where ν is the kinematic viscosity, $g' = g\Delta\rho/\rho$ is reduced gravity, $\Delta\rho$ is the difference in density between the upper and lower layer and ρ is the reference density. Hence the dominant wavelength of lithospheric root instabilities is

$$\lambda_d = \lambda_d^* b \quad (4)$$

and the characteristic time period for growth of the dominant instability is

$$\tau_d = \frac{\nu}{q_d^* g' b} \quad (5)$$

Now we consider a single instability of dominant wavelength. Since τ_d is a e -folding time, soon after $t = \tau_d$ the instability will achieve terminal downward velocity, detach from the upper layer and sink into the lower layer. Since fluid has been removed from the upper layer, the new thickness of the upper layer will be $< b$ above the site of the detachment, and the wavelength of the thinned patch of the upper layer will be $\sim \lambda_d$.

This situation resembles the original initial condition, and equation 3 with $w_0 \sim b$ predicts growth of the resulting instabilities. Thus, new instabilities will develop at horizontal distances $\pm \lambda_d$ relative to the initial instability. If this process repeats, the second-generation instabilities will grow, detach and trigger third-generation instabilities. Because this is a convective process, second-generation instabilities grow and detach before the thinned patch of upper layer above the initial instability can regain its original thickness by conductive cooling and thickening. Hence, the topographic gradient on the base of the upper layer will be greater above the outer edges of the second-generation instabilities, relative to the initial instability. Thus, third-generation and later instabilities will be initiated at progressively greater distances from the initial instability.

This simple physical model predicts that an initial Rayleigh-Taylor instability should initiate a chain of further instabilities, in which successive instabilities occur at horizontal distances of $\sim \lambda_d$ outboard of the initial instability with a periodicity of $\sim \tau_d$. The lateral propagation rate of this chain of events is therefore expected to scale as

$$U \sim \frac{\lambda_d}{\tau_d} \quad (6)$$

Substituting equations 4 and 5 gives

$$U \sim \lambda_d^* q_d^* \frac{g' b^2}{\nu} \quad (7)$$

which shows that U scales as b^2 . Typical values for U are plotted in Fig. 3a and shown in Extended Data Table 1a. The values of g' and b were estimated by fitting geotherms to xenolith P - T data (see below). The viscosity is expected to be of order 10¹⁵ m² s⁻¹ (refs^{53,54}), and we find that a value of 7×10^{15} m² s⁻¹ gives a good match between this scaling law, numerical models described below, and observed migration rates of kimberlite magmatism (Fig. 3a).

Thermo-mechanical models

Numerical forward models were conducted using the finite element code *ASPECT*⁵⁵ that solves the conservation equations of mass, energy, and momentum for materials with viscoplastic rheology⁵⁶. In particular we account for temperature and pressure dependent rheologies based on experimentally derived flow laws for dislocation and diffusion creep. Our model is kinematically driven through velocity boundary conditions at lateral sides, which leads to the self-consistent evolution of Rayleigh-Taylor instabilities at the base of the lithosphere. The model reproduces the formation of a narrow rift that is bounded at depth by steep LAB gradients resulting in pronounced rotational flow patterns²⁵. In further agreement with previous models, breakup is delayed due to rift migration⁵⁷.

We will now briefly describe the geometrical, mechanical and thermal setup of our geodynamic model, as well as its limitations. For a more detailed description of *ASPECT*'s functionalities and solution techniques we refer the reader to <https://aspect.geodynamics.org/manual.pdf>.

Xenolith geotherms

To estimate the typical thickness, temperature and density of the thermal boundary layer between the lithosphere and asthenosphere, for application in the delamination and melting calculations, we applied the numerical geotherm calculation approach of Mather et al. (2011)⁵³, which uses peridotite P - T estimates from various kimberlites. We utilized the *FIT-PLOT* programme (refs^{54,63}), which takes the thickness and thermal properties of the crust as inputs, and determines the thicknesses of the rigid lithospheric mantle and the basal lithospheric thermal boundary layer by minimizing the misfit between the calculated geotherm and the xenolith P - T data. Full details of this method and the xenolith datasets used are provided in ref.⁵³. Calculated geotherms and thermal boundary layer thicknesses are plotted in Extended Data Fig. 5. The total thickness of the thermal boundary layer is estimated to be 35 km. The corresponding thickness of the unstable viscous layer, b , that should be used in the analytical Rayleigh-Taylor instability models is approximately half this value, i.e., 17.5 km, since the lithosphere-asthenosphere boundary sits near the middle of the thermal boundary layer (Extended Data Fig. 5). The temperature change across the thermal boundary layer is $\sim 250^\circ\text{C}$. Thus, the mean density contrast that drives Rayleigh-Taylor instabilities is $\Delta\rho = \rho\alpha\Delta T/2 = 17\text{ kg m}^{-3}$, where $\alpha = 4 \times 10^{-5}\text{ C}^{-1}$ is the thermal expansivity, $\rho = 3,300\text{ kg m}^{-3}$ is the reference density and $\Delta T/2$ is the mean temperature difference relative to the asthenosphere. The corresponding reduced gravity is $g' = 0.05\text{ m s}^{-2}$. This driving density contrast is a lower bound because it does not include possible metasomatic density increases within the upper thermal boundary layer, but even without compositional effects it is sufficient to drive lithospheric delamination (Figs. 2 and 3a).

Melt calculations

We calculated the characteristic scale of melting associated with Rayleigh-Taylor instabilities at the base of thick lithosphere. Upwelling within the convective instabilities is sufficiently rapid for the temperature to be adiabatic. We assumed normal mantle temperature (potential temperature of $1,300^\circ\text{C}$) and calculated the degree of melting as a function of depth to the base of the rigid lithosphere (i.e. mechanical boundary layer), and also the water content of the primary melt, for adiabatic upwelling of mantle with bulk water contents of 0.1, 0.15 and 0.2 wt% (Extended Data Fig. 8a,c). We used the hydrous decompressional melting parameterization of Katz et al. (2003)⁶⁴ for these calculations. We then estimated the associated total melt productivity assuming a mean upwelling rate of 30 km Myr^{-1} , which is typical of the upwelling limbs of the convection cells in our numerical models (Extended Data Fig. 8b). Our calculations assume that the mantle source is enriched by volatiles, as has been proposed for the kimberlite mantle source^{2,3,42}. Such volatiles likely originate from incorporation of metasomatized keel, which contains hydrous phases such as phlogopite⁴⁷. Our calculations demonstrate that if decompression generates a melt productivity of 0.1 km Myr^{-1} across half the footprint of a convective instability with diameter 80 km,

The model comprises a domain of $2,000 \times 300\text{ km}$ and 800×120 elements in the x (horizontal) and y direction (depth), respectively. Quadratic shape functions of the finite element method are visualized as two piece-wise linear fields per element at an effective resolution of 1.25 km. The model comprises four layers: 20 km thick upper crust, 15 km thick lower crust, 125 km thick mantle lithosphere, and asthenosphere beneath 160 km depth. We use a wet quartzite⁵⁸ and wet anorthite⁵⁹ flow law for upper and lower crust, respectively, dry olivine rheology⁶⁰ for the mantle lithosphere, and wet olivine⁶⁰ for the asthenosphere. The model involves frictional strain softening, where we linearly reduce the friction coefficient with a factor of 0.25 for brittle strain between 0 and 1. For strains larger than 1, it remains constant. We also account for viscous strain softening by decreasing the viscosity derived from the ductile flow law with a factor of 0.25 between viscous strains 0 and 1. All rheological and mechanical model parameters are provided in Extended Data Table 1b. For visualization purposes, we distinguish a 30 km thick layer beneath some parts of the lithosphere as a simplified representation of variably metasomatized mantle. To initiate rifting in a predefined area, we use a 25 km thick upper crust and 100 km thin mantle lithosphere representing typical mobile belt conditions⁶¹.

We employ velocity boundary conditions with a total extension velocity of 10 mm per year. For simplicity, we keep the right-hand model side fixed, but we verified that the conclusions do not change if extension velocities are symmetrically distributed between the lateral boundaries. At the bottom boundary, we prescribe a constant vertical inflow of material that balances the outflow through the lateral model sides. The top boundary constitutes a free surface⁶².

Temperature boundary conditions feature a constant surface temperature of 0°C and a bottom temperature of $1,420^\circ\text{C}$. Lateral boundaries are thermally isolated. The initial temperature field of each model column results from the 1D thermal equilibrium defined by the boundary conditions, the crustal radiogenic heat contribution and the initial depth of the thermal LAB, i.e., the $1,350^\circ\text{C}$ temperature isotherm, which at first coincides with the compositional LAB. The sub-lithospheric temperature increases adiabatically with depth. To smooth the initial thermal gradient across the LAB, we equilibrate the entire thermal state of the model for 30 Myr before the onset of extension. All thermal parameters are listed in Extended Data Table 1b.

The following model limitations have to be kept in mind when interpreting the results. In this model, we focus on first-order thermo-mechanical processes and do not explicitly account for chemical alterations, melt generation and magma ascent. However, these processes are discussed in the context of Fig. 3a. For simplicity, we assume that the LAB is essentially flat on the 10^3 kilometre scale. Nonetheless, we conducted additional model runs with gradual changes in LAB depth and the conclusions remained the same. Additional effects like large-scale flow patterns related to mantle convection, the impingement of mantle plumes, and along-strike lithospheric heterogeneities may exert local effects on the formation of Rayleigh-Taylor instabilities that we have to neglect in our generic modelling strategy.

then a total magma flux of 250 km³ Myr⁻¹ could result. This flux is broadly consistent with existing estimates for kimberlite clusters³⁷ and demonstrate that the system is not limited by magma production at depth. The high volatile contents and low melting degrees in these simple calculations are generally in line with the calculations and petrological experiments on model systems, and it is well established that magma composition will evolve substantially during ascent (e.g. ref.⁷). Our calculations also show that melting can occur in the absence of plumes; yet more melting would be expected in cases where plumes are present.

Phase diagrams and phase equilibria

Modelling of phase relationships of carbonate-rich melts—thought to be parental to kimberlites—was undertaken using the open source *Perple_X* application suite⁶⁵ (available to download from <https://www.perplex.ethz.ch/>). We used the CMAS-CO₂ model system of Dalton and Presnall²⁸, which was developed specifically to study phase equilibria of mantle peridotite, which is in equilibrium with CO₂-bearing melts. The compositions used for the *Perple_X* calculations were the experimental melt compositions (JADSCM-7 and JADSCM-14) of Gudfinnsson and Presnall (2005)²⁷.

We used *Perple_X* to model the phase boundaries in the CMAS-CO₂ model system given by ref.²⁷. The shaded area (Fig. 3b) represents the experimentally determined region of carbonate-silicate melts (Gudfinnsson and Presnall²⁷), but phase relations in this region cannot be estimated using *Perple_X* because no adequate model for carbonate-silicate melts has been developed. However, the high-temperature (CO₂-free silicate melt) and low-temperature (onset of carbonate melting) boundaries of the carbonate-silicate melts (shaded area; Fig. 3b) can be located using *Perple_X*. Two different versions of the Holland and Powell (2004)⁶⁶ database were used to replicate the phase boundaries shown in figure 1 of Gudfinnsson and Presnall²⁷; this was done because end members for carbonate melts and solids were only available in *hp02ver.dat*, while updated end members for mafic melts and mineral phases are found in *hp633ver.dat*. Solution models used for both data sets were: O(HGP)-olivine, Opx(JH)-orthopyroxene, Grt(JH)-garnet, Sp(JH)-spinel; exclusive to *hp02ver.dat*: CcM(EF)-solid carbonate, LIQ(EF)-carbonate melt, Cpx(HP)-clinopyroxene; *hp633ver.dat*: Melt(JH)-silicate melt, Cpx(JH)-clinopyroxene. Details, including modifications, and original references for these solution models can be found in the text document *solution_model.dat*, available at: <https://www.perplex.ethz.ch/perplex/datafiles/>.

To plot estimated *P-T* conditions of Ilherzolite/peridotite nodules (Fig. 3b), it was necessary to convert some depths from published compilations to pressures, which was done using

$$P = \rho \times g \times h \quad (8)$$

where ρ is the density of the lithosphere, g is acceleration due to gravity and h is the depth. In our calculations, we took $\rho = 3,200 \text{ kg m}^{-3}$, based on an assumed lithospheric thickness of 180 km, comprising a crustal thickness of 45 km and crustal-

density of 2,750 kg m⁻³ (ref.⁶⁷), and a lithospheric thickness of 135 km and density of 3,300 kg m⁻³ (i.e., using a middle value from ref.⁶⁸).

Statistical analysis of isotope variations

We compiled existing data to assess whether any temporal changes in kimberlite geochemistry are detectable during the inferred sharp reduction in lithospheric thickness in the Kaapvaal Craton at c. 117–108 Ma (ref.⁴⁰), which is hypothesised to be a consequence of delamination. Here, we first analyzed whole rock (⁸⁷Sr/⁸⁶Sr)_i, (¹⁴³Nd/¹⁴⁴Nd)_i and (²⁰⁶Pb/²⁰⁴Pb)_i from Smith et al. (1986)⁴⁷, updating the radiometric ages of the kimberlites where necessary. Because kimberlites are particularly susceptible to syn- and post-emplacement alteration by crustal fluids, whole rock Sr and Pb isotope data may not provide a very accurate record of mantle source compositions⁶⁹. Therefore, we also studied the temporal variation in perovskite initial ⁸⁷Sr/⁸⁶Sr ratios⁷⁰ and whole rock ¹⁴³Nd/¹⁴⁴Nd ratios⁷¹ in Cretaceous southern African kimberlites (Extended Data Fig. 9). The plots show the Sr and Nd isotope compositions of the MARID (Mica-Amphibole-Rutile-Ilmenite-Clinopyroxene) end-member defined from kimberlite xenoliths and is thought to derive from a lithospheric mantle source that has been variably contaminated by recycled crustal components, possibly during a subduction event at ~2.9–3.2 Ga⁷². The plots also show the composition of the kimberlite melt end-member of ref.⁷², largely defined from analyses of PIC (Phlogopite-Ilmenite-Clinopyroxene) kimberlite xenoliths. This end-member is interpreted to reflect a mantle source that has been metasomatized by kimberlite melts⁷² and it is interesting to note that this end-member has very similar Sr, Nd and Pb isotope compositions as average Cretaceous to Cenozoic African carbonatites⁷³.

We next used conjugate partitioned recursion (CPR) to evaluate the potential presence of step changes in the above isotopic datasets (Extended Data Fig. 9). This iterative algorithm uses binary partitioning by marginal likelihood and conjugate priors (conjugate partitioned recursion) to identify an unknown number of change-points⁷⁴. If the marginal likelihood favours a change-point model, then the algorithm defines a change point and two-sigma uncertainty bounds of the two averages before and after the change point⁷⁴. In applying the CPR algorithm to the perovskite (⁸⁷Sr/⁸⁶Sr)_i and whole rock (⁸⁷Sr/⁸⁶Sr)_i, (¹⁴³Nd/¹⁴⁴Nd)_i and (²⁰⁶Pb/²⁰⁴Pb)_i datasets, we identified a prominent change-point at 114 Ma for all of the isotopic proxies, except (¹⁴³Nd/¹⁴⁴Nd)_i, which occurs between 114–100 Ma, and ϵ Nd, which occurs between 118–114 Ma (Extended Data Figure 9). The step changes in Sr and Nd isotope systematics at ~114 Ma are compatible with initial melting of metasomatized lithospheric mantle prior to, and during, detachment of the cratonic mantle keel. This is then followed by eruption of melts exhibiting a stronger asthenospheric signature, but that nevertheless retain a sufficient carbonate burden to generate diamond-bearing kimberlites.

Additional references are cited in Extended Data^{75,76}.

Data availability

All data generated or analyzed during this study will be provided in the online version of this article and in Extended Data Table 1.

Code availability

More details on the computational methods and tools used for this study are available from the corresponding author (Thomas.Gernon@noc.soton.ac.uk) upon request.

51. R. D. Müller, M. Seton, S. Zahirovic, S. E. Williams, K. J. Matthews, N. M. Wright, G. E. Shephard, K. T. Maloney, N. Barnett-Moore, M. Hoesenipour, D. J. Bower, and J. Cannon. Ocean basin evolution and global-scale plate reorganization events since Pangea breakup. *Annual Review of Earth and Planetary Sciences*, 44(1):107–138, 2016.
52. R. L. Evans, A. G. Jones, X. Garcia, M. Muller, M. Hamilton, S. Evans, C. J. S. Fourie, J. Spratt, S. Webb, H. Jelsma, and D. Hutchins. Electrical lithosphere beneath the Kaapvaal craton, southern Africa. *Journal of Geophysical Research: Solid Earth*, 116(B4):B04105, 2011.
53. K. A. Mather, D. G. Pearson, D. McKenzie, B. A. Kjarsgaard, and K. Priestley. Constraints on the depth and thermal history of cratonic lithosphere from peridotite xenoliths, xenocrysts and seismology. *Lithos*, 125(1):729–742, 2011.
54. D. McKenzie, J. Jackson, and K. Priestley. Thermal structure of oceanic and continental lithosphere. *Earth and Planetary Science Letters*, 233(3):337–349, 2005.
55. T. Heister, J. Dannberg, R. Gassmüller, and W. Bangerth. High accuracy mantle convection simulation through modern numerical methods—II: realistic models and problems. *Geophysical Journal International*, 210(2):833–851, 2017.
56. A. Glerum, C. Thieulot, M. Fraters, C. Blom, and W. Spakman. Non-linear viscoplasticity in ASPECT: benchmarking and applications to subduction. *Solid Earth*, 9(2):267–294, 2018.
57. S. Brune, C. Heine, M. Pérez-Gussinyé, and S. V. Sobolev. Rift migration explains continental margin asymmetry and crustal hyper-extension. *Nature Communications*, 5(1):4014, 2014.
58. E. H. Rutter and K. H. Brodie. Experimental grain size-sensitive flow of hot-pressed Brazilian quartz aggregates. *Journal of Structural Geology*, 26(11):2011–2023, 2004.
59. E. Rybacki, M. Gottschalk, R. Wirth, and G. Dresen. Influence of water fugacity and activation volume on the flow properties of fine-grained anorthite aggregates. *Journal of Geophysical Research: Solid Earth*, 111(B3), 2006.
60. G. Hirth and D. Kohlstedt. Rheology of the upper mantle and the mantle wedge: A view from the experimentalists. In J. Eiler, editor, *Inside the Subduction Factory*, pages 83–105. American Geophysical Union (AGU), 2004.
61. M. E. Pasyanos, T. G. Masters, G. Laske, and Z. Ma. LITHO1.0: An updated crust and lithospheric model of the Earth. *Journal of Geophysical Research: Solid Earth*, 119(3):2153–2173, 2014.
62. I. Rose, B. Buffett, and T. Heister. Stability and accuracy of free surface time integration in viscous flows. *Physics of the Earth and Planetary Interiors*, 262:90–100, 2017.
63. D. McKenzie and M. J. Bickle. The volume and composition of melt generated by extension of the lithosphere. *Journal of Petrology*, 29(3):625–679, 1988.
64. R. F. Katz, M. Spiegelman, and C. H. Langmuir. A new parameterization of hydrous mantle melting. *Geochemistry, Geophysics, Geosystems*, 4(9):1073, 2003.
65. J. A. D. Connolly. Computation of phase equilibria by linear programming: A tool for geodynamic modeling and its application to subduction zone decarbonation. *Earth and Planetary Science Letters*, 236(1):524–541, 2005.
66. T. J. B. Holland and R. Powell. An internally consistent thermodynamic data set for phases of petrological interest. *Journal of Metamorphic Geology*, 16(3):309–343, 1998.
67. I. M. Artemieva and A. Shulgin. Making and altering the crust: A global perspective on crustal structure and evolution. *Earth and Planetary Science Letters*, 512:8–16, 2019.
68. B. Xia, H. Thybo, and I. M. Artemieva. Lithosphere mantle density of the North China Craton. *Journal of Geophysical Research: Solid Earth*, 125(9):e2020JB020296, 2020.
69. D. G. Pearson, J. Woodhead, and P. E. Janney. Kimberlites as geochemical probes of Earth’s mantle. *Elements*, 15(6):387–392, 2019.
70. J. Woodhead, J. Hergt, D. Phillips, and C. Paton. African kimberlites revisited: In situ Sr-isotope analysis of groundmass perovskite. *Lithos*, 112:311–317, 2009.
71. G. M. Nowell, D. G. Pearson, D. R. Bell, R. W. Carlson, C. B. Smith, P. D. Kempton, and S. R. Noble. Hf isotope systematics of kimberlites and their megacrysts: New constraints on their source regions. *Journal of Petrology*, 45(8):1583–1612, 2004.
72. A. Fitzpayne, A. Giuliani, R. Maas, J. Hergt, P. Janney, and D. Phillips. Progressive metasomatism of the mantle by kimberlite melts: Sr–Nd–Hf–Pb isotope compositions of MARID and PIC minerals. *Earth and Planetary Science Letters*, 509:15–26, 2019.
73. K. Bell and G. R. Tilton. Nd, Pb and Sr isotopic compositions of east african carbonatites: Evidence for mantle mixing and plume inhomogeneity. *Journal of Petrology*, 42(10):1927–1945, 2001.
74. G. Jensen. Closed-form estimation of multiple change-point models. *PeerJ Preprints*, 1:e90v3, 2013.
75. A. M. Goodwin. *Principles of Precambrian Geology*. Academic Press, 1996.
76. D.L. Turcotte and G. Schubert. *Geodynamics*. Cambridge University Press, 2 edition, 2002.

Supplementary Files

This is a list of supplementary files associated with this preprint. Click to download.

- [ModelEvolutionAnimation103d.mp4](#)
- [ExtendedData.pdf](#)